The Company of Biologists

RESEARCH ARTICLE

Substrate adhesion determines migration during mesenchymal cell condensation in chondrogenesis

Ignasi Casanellas[1,2,3,*], Hongkai Jiang[4], Carolyn M. David[5], Yolanda Vida[6,7], Ezequiel Pérez-Inestrosa[6,7], Josep Samitier[1,2,3] and Anna Lagunas[1,3,‡]

ABSTRACT

Mesenchymal condensation is a prevalent morphogenetic transition that is essential in chondrogenesis. However, the current understanding of condensation mechanisms is limited. *In vivo*, progenitor cells directionally migrate from the surrounding loose mesenchyme towards regions of increasing matrix adherence (the condensation centers), which is accompanied by the upregulation of fibronectin. Here, we focused on the mechanisms of cell migration during mesenchymal cell condensation and the effects of matrix adherence. Dendrimer-based nanopatterns of the cell-adhesive peptide arginine-glycine-aspartic acid (RGD), which is present in fibronectin, were used to regulate substrate adhesion. We recorded collective and single-cell migration of mesenchymal stem cells, under chondrogenic induction, using live-cell imaging. Our results show that the cell migration mode of single cells depends on substrate adhesiveness, and that cell directionality controls cell condensation and the fusion of condensates. Inhibition experiments revealed that cell–cell interactions mediated by N-cadherin (also known as CDH2) are also pivotal for directional migration of cell condensates by maintaining cell–cell cohesion, thus suggesting a fine interplay between cell–matrix and cell–cell adhesions. Our results shed light on the role of cell interactions with a fibronectin-depositing matrix during chondrogenesis *in vitro*, with possible applications in regenerative medicine.

This article has an associated First Person interview with the first author of the paper.

KEY WORDS: Cell migration, Mesenchymal condensation, Nanopatterned substrates, Arginine-glycine-aspartic acid, RGD, Chondrogenesis

[1]Nanobioengineering group, Institute for Bioengineering of Catalonia (IBEC), Barcelona Institute of Science and Technology (BIST), 08028 Barcelona, Spain. [2]Department of Electronics and Biomedical Engineering, Faculty of Physics, University of Barcelona (UB), 08028 Barcelona, Spain. [3]Biomedical Research Networking Center in Bioengineering, Biomaterials, and Nanomedicine (CIBER-BBN), 28029 Madrid, Spain. [4]Biomedical Engineering, Vanderbilt University School of Engineering, Vanderbilt University, Nashville, TN 37235-1826, USA. [5]P.C. Rossin College of Engineering and Applied Science, Lehigh University, Bethlehem, PA 18015, USA. [6]Universidad de Málaga - IBIMA, Departamento de Química Orgánica, Campus de Teatinos, 29071 Málaga, Spain. [7]Laboratory of Dendrimers, Biomimetics and Photonics, Centro Andaluz de Nanomedicina y Biotecnología-BIONAND, Parque Tecnológico de Andalucía, 29590 Campanillas, Málaga, Spain. *Present address: Department of Physiology and Biophysics, University of California, Irvine, 92697 CA, USA.

‡Author for correspondence (alagunas@ibecbarcelona.eu)

I.C., 0000-0002-5264-169X; Y.V., 0000-0002-7004-4629; J.S., 0000-0002-1140-3679; A.L., 0000-0002-0936-3401

INTRODUCTION

Condensations of mesenchymal cells are present during development of many tissues and organs, including cartilage and bone. In osteochondral development, condensation is a transient phase in which the size and position of each cartilage anlage is defined (DeLise et al., 2000). An abnormal condensation process results in developmental defects (Atchley and Hall, 1991; Giffin et al., 2019). Several inductive epithelial signaling molecules have been identified as initiators of mesenchymal condensation (Giffin et al., 2019). Transforming growth factor β (TGF-β) induces the condensation of mesenchymal cells at high density through the upregulation of the adhesive extracellular glycoprotein fibronectin (FN) (Miura and Shiota, 2000; Singh and Schwarzbauer, 2012). However, the mechanisms orchestrating cell interactions with an FN-depositing matrix that promote cell gathering during mesenchymal cell condensation and the growth of condensates remain largely unexplored.

It has been proposed that condensation results from extracellular matrix (ECM)-driven translocation and directional migration of cells from the surrounding loose mesenchyme to the condensed region (Newman and Tomasek, 1996). During condensation, active mesenchymal cell migration towards condensation centers (regions of increased cell–FN adhesive interactions) causes an increase in mesenchymal cell-packing density without cell proliferation (Janners and Searls, 1970), in which cells acquire epithelioid properties by the upregulation of cell–cell adhesion molecules (Oberlender and Tuan, 1994). Cell gathering promotes the establishment of cell–cell contacts through the cell adhesion molecules N-cadherin (also known as CDH2, referred to hereafter as N-Cad), neural adhesion molecule (N-CAM, also known as NCAM1) (Widelitz et al., 1993), and gap junctions (GJs) that facilitate cell coordination within the cohort (Coelho and Kosher, 1991). The extent of mesenchymal cell condensation has been related to the level of cell differentiation towards chondrogenesis (Evans and Tuan, 1988; San Antonio and Tuan, 1986).

In recent years, our group has developed a dendrimer-based nanopatterning technique using arginine-glycine-aspartic acid (RGD)-functionalized polyamidoamine (PAMAM) generation 1 (G1) dendrimers that allow us to control the local surface adhesiveness at the nanoscale on large surface areas, thus being compatible with standard cell culture protocols (Casanellas et al., 2018; Lagunas et al., 2014). By using different solution concentrations of the dendrimers, we have created different nanopattern configurations by adsorption with a liquid-like order on low-charged surfaces. Although each dendrimer of 4–5 nm in diameter contains eight copies of RGD, due to steric effects, a dendrimer can solely interact with one integrin receptor of ∼10 nm diameter (Lagunas et al., 2014; Xiong et al., 2002). Thereby, dendrimer configuration on the surface matches the adhesive sites for integrin interaction. We have used this method to produce

different nanopatterns on poly(L-lactic acid), naming them according to the percentage of surface area containing inter-dendrimer distances below the 70 nm threshold, which is required for an efficient cell adhesion on stiff surfaces: S_{90} (90%, high adherence), S_{45} (45%, intermediate adherence) and S_{18} (18%, low adherence) (Arnold et al., 2004; Lagunas et al., 2017; Oria et al., 2017). We have observed that nanopatterns effectively sustain cell culture for several days and that, under chondrogenic induction, human adipose-derived mesenchymal stem cells (hASCs) form condensations on all the nanopatterns (Lagunas et al., 2017).

Here, we focus on the on the mechanisms of cell migration during mesenchymal cell condensation and their dependence on matrix adherence. With this aim, we used live-cell imaging to observe the first 40 h of condensation of hASCs under chondrogenic stimuli on the nanopatterns. We recorded single and collective cell migration dynamics and conducted cell tracking and immunofluorescence analysis. We observed that the cell migration mode of single cells depended on substrate adhesiveness, changing from amoeboid-like to more mesenchymal with increasing adhesion. Cells on S_{90} nanopatterns showed traits from both modes of migration, preserving amoeboid features that facilitate migration but, at the same time, having enhanced directional movement, larger protrusions and reduced contact inhibition of locomotion (CIL), which favors condensation. Our results demonstrate that cell directionality, not velocity, controls the condensation of single cells and the fusion of condensates, and suggest that this is modulated by integrin-mediated adhesion. In addition, inhibition of cell–cell interactions showed that N-Cad-mediated cell cohesiveness is necessary for the directional migration of condensates on S_{90} nanopatterns, thus indicating that a fine balance between substrate adhesion and cell–cell adhesions regulates condensation and the growth of cell condensates. Taken together, these results highlight the relevance of the fine tuning of migration characteristics through cell–substrate interactions for an efficient condensation and further chondrogenesis *in vitro*, with implications in cartilage tissue engineering approaches.

RESULTS
hASCs adapt their migration mode to the adhesive properties of the substrate

hASCs were seeded on the nanopatterned substrates (S_{18}, S_{45} and S_{90}) in chondrogenic culture medium to induce mesenchymal cell condensation. Pristine non-patterned susbtrates (S_0) and FN-coated substrates (S_{FN}) were chosen as representatives of non-adherent (Zhu et al., 2004) and highly adherent surfaces, respectively. We first checked the number of adhered cells on each substrate, which as expected, increased with the RGD ligand density (Fig. 1A). Cell movement was tracked using fluorescence live-cell imaging for 40 h. In the absence of symmetry-breaking gradients, mesenchymal cells are expected to migrate randomly (persistent random walks, PRWs), dynamically switching between fast translocation and slow rotation, combining elongated and rounded morphologies, respectively (Wu et al., 2015). We observed that, while single cells on S_{FN} adhered and spread within the first 48 min after cell seeding, single cells on the nanopatterns and on the S_0 control preserved their rounded morphology (Fig. 1B; Fig. S1). Differences in cell spreading conditioned the cell migration mode. Cells on S_{FN} displayed a typical mesenchymal migration, with elongated spindle-like morphologies and a protruding leading edge, which was rich in actin (Fig. 1C), and cells on S_0 and the nanopatterns exhibited amoeboid-like migration presenting rounded irregular morphologies that underwent transient expansion and contraction cycles with protruding

filopodia (Fig. 1D). Cell spreading also influenced actin network configuration, which was organized in stress fibers in cells on S_{FN}, whereas single cells on S_0 and on the nanopatterns displayed a cortical actin organization (Casanellas et al., 2020) that concentrated at the rear part of the cell during migration (Fig. 1E).

Amoeboid migration of slow mesenchymal cells has been described previously for cells on substrates with adhesion levels that impede cell binding; this has been attributed to the absence of focal adhesions (FAs) (Liu et al., 2015). Accordingly, we observed that in amoeboid migrating cells, β1 integrin (also known as ITGB1) and the FA adaptor protein paxillin (Pax) were homogeneously distributed, and no FAs were formed. Nevertheless, in these samples (both S_0 and the nanopatterns), Pax-rich FAs could be observed along the perimeter of spreading cells already forming cell aggregates (Fig. 1F), indicating that integrin-based adhesion was not completely inhibited on these substrates. Moreover, the presence of filopodia during transient expansion in amoeboid migrating single cells and in cell–cell interactions, suggested the engagement of integrin receptors (Renkawitz et al., 2009). Quantification of the length of filopodia for cells on S_0 and on the nanopatterns demonstrated that cells on S_{90} generate significantly longer protrusions (Fig. S2), indicating that cells are sensitive to the RGD integrin-ligand density on the substrates. hASCs on S_{FN} form FAs (Lagunas et al., 2017), thus supporting the traction forces necessary for mesenchymal migration.

Cells migrating on high-adherence substrates show a more directional movement

Quantification of the mean track velocity revealed that cells on mid-adherence nanopatterns (S_{45}) migrated significantly faster ($\sim$0.6 μm min^{-1}) than cells on the other substrates (Fig. 2A). This agrees with previous reports showing a biphasic dependence of cell migration velocity, in which a maximal migration rate can be found for an intermediate level of cell–substrate adhesiveness (DiMilla et al., 1993). To quantify directionality, we examined the cell track directness, which was calculated as the ratio of the Euclidean distance (the shortest straight distance between the start and end points of the cell trajectory) and the total trajectory covered by the cell. A value of directness closer to 1 indicates a more directional movement, whereas lower values reveal a more winding path (values equal to 0 are attributed to static cells). Directness increased with substrate adhesiveness, and similar values were obtained for cells on S_{18} and S_{45} substrates (Fig. 2B). The more directional migration with increased substrate adhesiveness could be also qualitatively appreciated when plotting the cell trajectories (Fig. S3). Moreover, the turning angles between consecutive frames obtained for cells on S_0 showed random cell movement, with all angles having a similar probability. With increasing local RGD density, cell motility progressively evolved towards a more directional migration, as shown by the higher proportion of turning angles at low values (Fig. 2C). The calculated mean squared displacement (MSD) of the cell trajectories also reflected the increase in directionality of the movement with the increase in adhesion of the substrate. MSD is a measure of the spatial extent of the region explored by the cells. When measured over time, the MSD showed a steeper increase with increasing local ligand density, due to the higher directional persistence in cell migration (Fig. 2D). Thus, our results show that cells on more adherent substrates present a more directional movement that allows them to move over longer distances despite their lower migration rate.
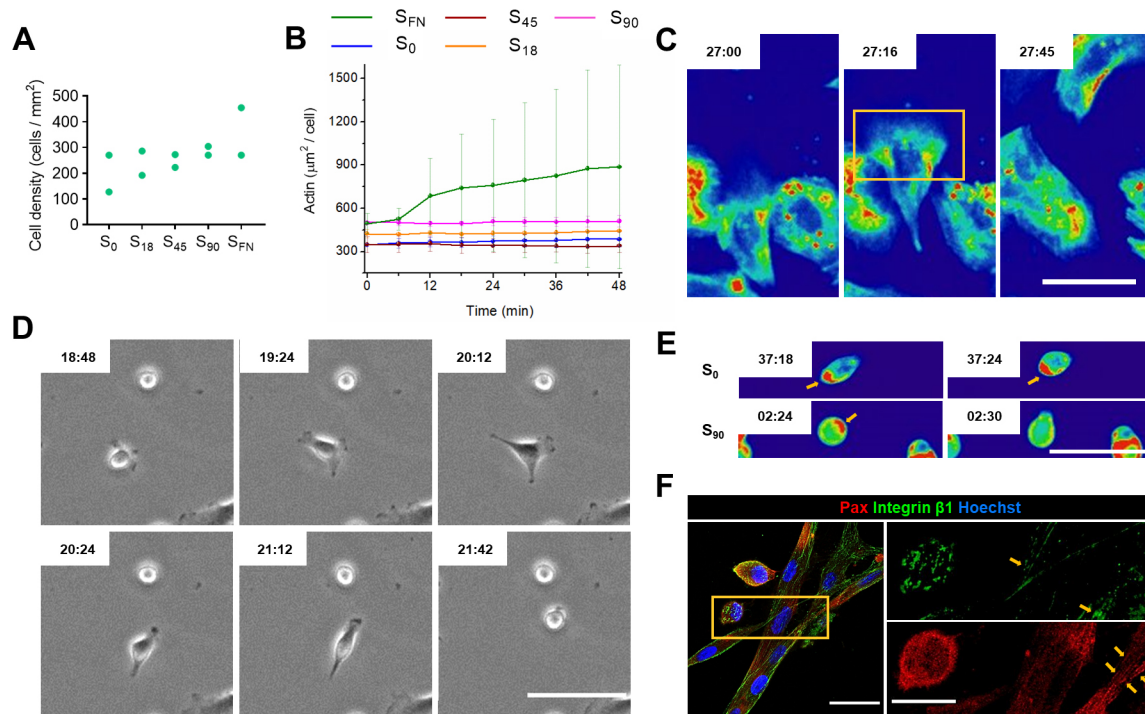
Fig. 1. hASCs under chondrogenic stimuli adapt their migration mode to the environment. (A) Quantification of initial cell density of adhered hASCs after seeding, $128 \leq n \leq 455$ cells. $N=2$ experiments. (B) Quantification of the cell spreading area, as determined from actin staining (SiR-actin), during the first 48 min after cell seeding. $n=9$, data are presented as the mean±s.e.m. (C) Time-lapse intensity color map representation of actin staining (SiR-actin) of cells on S_{FN}, showing the actin-rich leading front (yellow box) of a mesenchymal migrating cell. Maximum and minimum actin intensity values are shown in red and blue, respectively. Images are representative of 30 cells. Scale bar: 75 μm. (D) Time-lapse phase-contrast images of an amoeboid migrating cell on S_{90} switching between rounded and extended morphologies. Images are representative of 30 cells. Scale bar: 100 μm. (E) Time-lapse intensity color map representation of actin staining of cells on S_0 and S_{90} showing cortical actin concentration at the rear part of the cell (yellow arrows) during amoeboid migration. Maximum and minimum actin intensity values are shown in red and blue, respectively. Images are representative of 30 cells. Scale bar: 80 μm. In C–E, the time indicated in each panel (in hours and minutes) is the time from seeding and the start of imaging. (F) Representative immunofluorescence images of cells on S_{90}. Rounded single cells and spread interacting cells can both be observed during cell tracking. Images on the right correspond to the region highlighted by a yellow box in the left-hand image and show that FAs are only present in the spread groups of cells (yellow arrows), while integrin β1 (green) and Pax (red) appear diffuse within the cytosol in the amoeboid migrating cells. Nuclei were stained using Hoechst 33342. Images are representative of 30 cells. Scale bars: 30 μm (left), 15 μm (right).

Simulated whole-cell migration

To account for cell–substrate interactions, we adapted the model of whole-cell simulation of cell migration developed previously by Odde and co-workers (Chan and Odde, 2008; Klank et al., 2017). Since each dendrimer of 4–5 nm diameter is able to bind just one integrin molecule (Lagunas et al., 2014), we modeled the substrate as discrete integrin binding sites defined by the adsorbed dendrimers. The individual integrin–RGD dendrimer bonds and the adaptor proteins were modeled as molecular clutches linking F-actin to the substrate, with the mechanical resistance to myosin-driven F-actin retrograde flow regulated through the stiffness of the clutches and the dendrimer adsorption force (Fig. 3A). As in previous works (Klank et al., 2017), we maintained a constant number of actin motors and we varied the number of clutches in proportion to the variation in dendrimers on the different nanopatterns, previously determined using atomic force microscopy (AFM) analysis (Lagunas et al., 2017) . We set the number of clutches to 20 for S_0 and set the number of clutches equal to the number of motors for S_{FN}. We obtained simulated cell trajectories for the different substrates (Fig. 3B), from which the MSD and the random motility coefficient (RMC) were calculated (Fig. 3C,D). However, the MSD profiles obtained from the simulation did not reproduce the experimental data (Fig. 3D, compare to experimental

data in Fig. 2D). Since MSD is a function of both the mean velocity and persistence of cell motility (Yeoman and Katira, 2019), discrepancies between the calculated and experimental values could be attributed to the predominant effect of directional persistence, as observed in the experimental data, which would lead to deviations from the PRW model.

Cell condensate formation and collective cell migration

Immediately after seeding, cells on S_0 and on the nanopatterns were observed to start aggregating into condensates (Movies 1–4 for S_0, S_{18}, S_{45} and S_{90}, respectively). Conversely, cells on S_{FN} quickly developed a compact monolayer (Movie 5), from which no clusters of cells appeared until 5 days of chondrogenic induction, as reported previously (Lagunas et al., 2017). During cell condensate formation, cells interacted with each other and generated stable adhesions. The number of cells and the velocity and directionality of migration in a multicellular environment will affect the number of cell–cell encounters and thus the chances for condensation to ensue. We quantified cell–cell merge events, defined as instances of two tracks reaching a nucleus–nucleus distance of less than 30 μm. The rate of merge events per track was equal or very similar for cells on S_0, S_{18} and S_{90} substrates (means of 0.22–0.23 merge events h^{-1}) but was significantly higher for cells on S_{45} (0.35 events h^{-1})
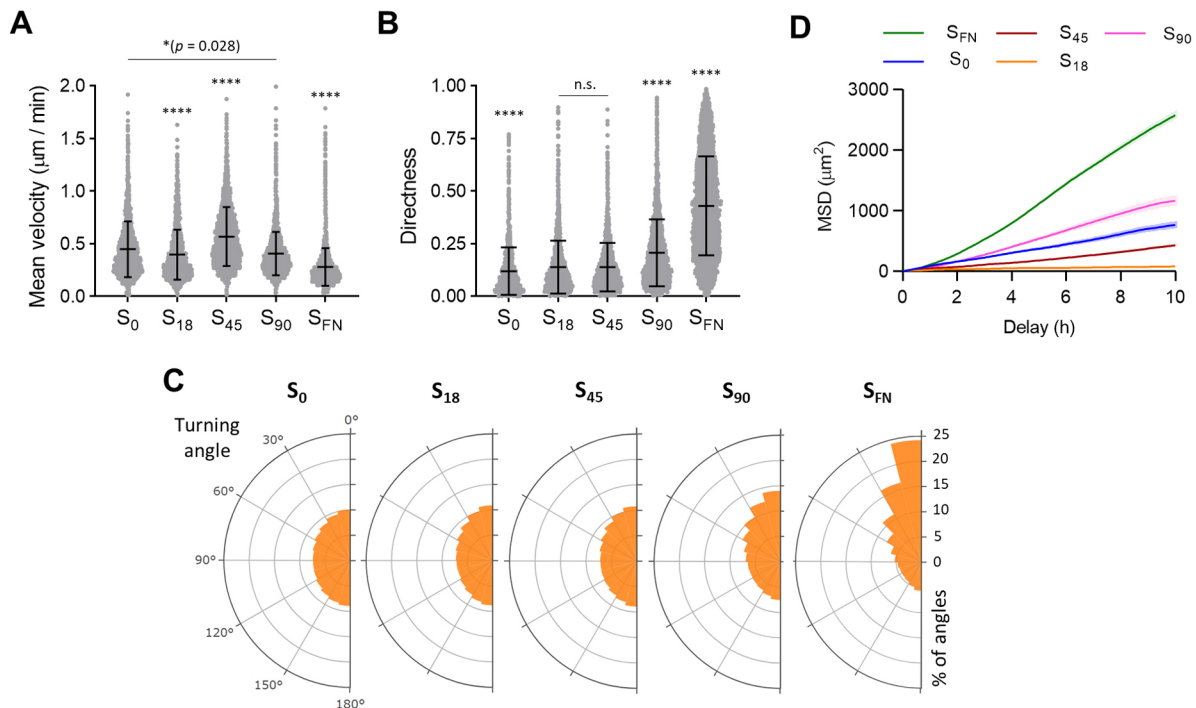
Fig. 2. Single cells migrate more directionally with increasing the adhesiveness of the substrate. (A) Quantification of mean velocity of single cells on the indicated substrates. (B) Quantification of track directness. Results in A and B are presented as the mean±s.d. of $2387 \leq n \leq 7424$ tracks. (C) Polar histograms of turning angles in single-cell tracks on the indicated substrates; $309{,}555 \leq n \leq 980{,}940$ turns. (D) MSD for cells migrating on each of the substrates. Results are the mean±s.e.m. $n=384$ tracks. Data are from at least two independent experiments, with data from all experiments used in the calculations. Statistical significance was determined by a Kruskal–Wallis test with Dunn's multiple-comparison post hoc test. *$P<0.05$; ****$P<0.0001$; n.s., not significant.

(Fig. 4A), thereby suggesting that the number of merge events is facilitated by a higher mean velocity on the substrates, and that there are more chances for cells on S_{45} nanopatterns to initiate condensation.

Since cells on S_0 and on the nanopatterns retained their rounded morphology during individual cell migration, the increase in the spreading area observed during the first 15 h of cell tracking (Fig. 4B, area between dashed lines) can be attributed to cell condensation. Quantification of the spreading area from actin staining revealed that the growth rate of the cell condensates, measured as the slope of the curves in Fig. 4B, was faster on S_{90} (see Table S1 for fitting parameters and dataset comparison tests). This higher growth rate, which did not correspond with the number of merge events, could be caused either by the formation of more condensates on the sample and/or by condensates growing larger. Previous results have shown that S_{90} and S_{45} nanopatterns produce condensates of similar projected areas after 1 day of culture (Lagunas et al., 2017). Fig. 4C shows that in the same time, more condensates were formed on S_{90} than on S_{45}, indicating that merge events on S_{90} nanopatterns, although less frequent, are more efficient in terms of cell condensate formation, whereas on S_{45} a higher proportion of cell encounters do not lead to condensation.

We analyzed the migration dynamics of multicellular cell condensates on the different substrates. In analogy to our single-cell migration analysis, whole condensates were segmented and tracked (Fig. 4D), starting at 20 h of imaging. Cell condensate trajectories are shown in Fig. 4E. We found that substrate adhesiveness had similar effects on collective cell migration as on single cells. The Euclidean distance of migration was observed to increase with increasing substrate adhesiveness (Fig. 4F), indicating

a more directional cell movement, which was supported by measurements of the mean velocity and track directness (Fig. 4G and H, respectively). Cell condensates on S_{45} and S_{90} nanopatterns had a similar migration rate ($\sim 0.4\ \mu m\ min^{-1}$), whereas the directionality of the movement was significantly higher on the S_{90} substrate, as was also apparent in the quantification of turning angles (Fig. S4). The rate of migration was significantly slower for cell condensates on all the substrates compared to that of single-cell migration, although the shape of the curve of the mean velocity against substrate adhesiveness was preserved (Fig. 4I). Track directness values (Fig. 4J) show that the directionality of the movement was very similar in single-cell migration and in condensate migration.

During live-cell imaging, we observed several instances of two or more cell condensates coming into contact and then fusing through a coalescence-like mechanism, leading to the formation of bigger structures (Movies 6 and 7). We have previously observed that the size of cell condensates increases during the first 5 days of chondrogenic induction (Lagunas et al., 2017), which could be the result of incorporation of cells in an existing cell condensate and/or merging of cell condensates. On S_{90} nanopatterns, there was a significant decrease in the number of cell condensates from day 1 to day 5 of culture (Fig. 4C). Considering that on S_{90} nanopatterns the condensates are stable for up to 14 days in culture (Casanellas et al., 2020), we attributed the decrease in their number to the occurrence of merging events, which were about twice as frequent on S_{90} nanopatterns than on the rest of the substrates (Fig. 4K). This correlates with increase in size of cell condensates previously observed from day 1 to day 5 of culture on the nanopatterns (Lagunas et al., 2017).
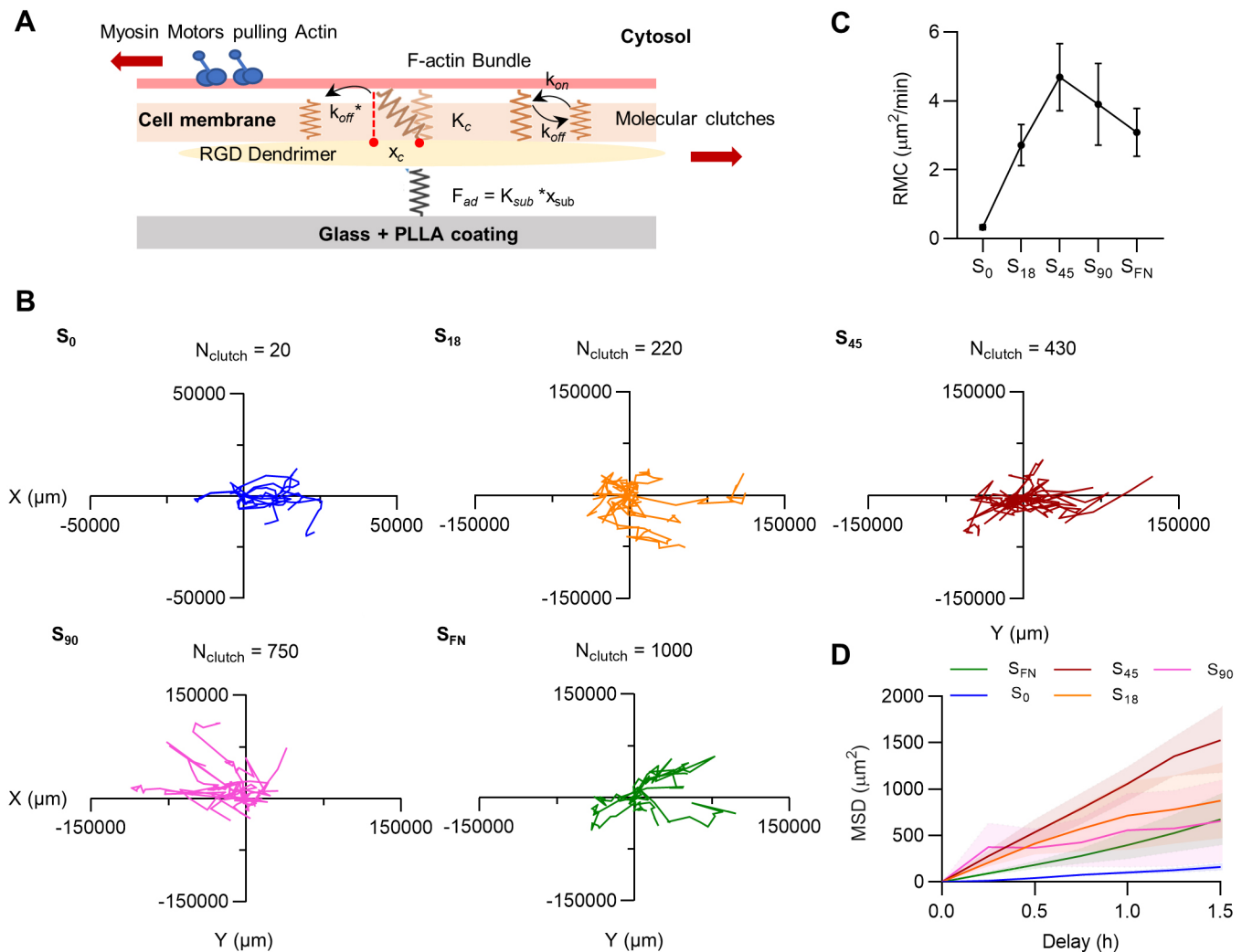
Fig. 3. Single-cell migration simulation. (A) Schematics of a motor–clutch module. Myosin motors pull the F-actin filament bundle retrogradely causing the displacement of the clutches and building tension. The molecular clutches can reversibly engage the F-actin bundle with rates k_{on} and k_{off} to resist retrograde flow. During loading, the molecular clutches are displaced till they fail at x_c with a k_{off}^* rate, which is force dependent. The mechanical stiffness of the clutches, K_c, and the adsorption force of the dendrimers ($F_{ad}=K_{sub}*x_{sub}$) will determine the mechanical resistance to loading. K_{sub}, stiffness of the substrate; x_c, strains of the clutches during loading; x_{sub}, local substrate strain. (B) Plot of representative single-cell trajectories obtained from 5 h simulation and a constant motor number per cell, which was maintained at 1000. The number of clutches (N_{clutch}) on the nanopatterned substrates was calculated by setting 750 clutches for S_{90} and decreasing this number for S_{45} and S_{18} in the same proportion as the decrease in number of dendrimers inferred from AFM image thresholds (data not shown). N_{clutch} was set at 20 for S_0 and at 1000 for S_{FN}. (C,D) Calculated RMC (C) and MSD (D) from the simulated cell trajectories. Results are the mean±s.e.m. of n=10 simulated cells.

Blocking cell–substrate and cell–cell interactions

Our tracking results suggest that substrate adhesion on S_{90} nanopatterns induces an intermediate mode of migration, where cells exhibit most common amoeboid migration traits but present higher directional persistence, which could be advantageous for cell condensate formation and growth. We analyzed migration and condensation on the different substrates under three types of pharmacological intervention that impair certain cell–substrate and cell–cell interactions: in-solution RGD dendrimers, ADH1 peptides and 18β-glycyrrhetinic acid (18βGA). Addition of RGD peptides to the culture medium impairs integrin clustering (Cluzel et al., 2005; Wang et al., 2010); we thus expected that RGD dendrimers in solution would have a similar effect, hampering integrin interaction with substrate-adsorbed ligands by competition. ADH1 is a cyclic pentapeptide that contains a HAV sequence, which binds to the adherens junction protein N-Cad (Erez et al., 2004; Williams et al.,

2000), thus blocking it when added in cell culture (Madl et al., 2017; Madl et al., 2019; Shintani et al., 2008). Phosphorylation of gap junctional connexin proteins regulates several aspects of GJ intercellular communication, including GJ formation, gating and turnover (Pogoda et al., 2016; Solan and Lampe, 2014, 2018). 18βGA is a saponin that induces disassembly of GJ plaques through connexin dephosphorylation (Böhmer et al., 2001; Guan et al., 1996).

We imaged single-cell and multicellular cluster dynamics on S_{90} substrates under each of the pharmacological treatments (Movies 8–10 correspond to in-solution RGD dendrimer, ADH1 and 18βGA treatments, respectively). All treatments caused a significant reduction in the directional persistence of single-cell movement, although integrin blockage had a stronger effect: a 2-fold decrease in directness was measured upon the addition of RGD dendrimers in solution (Fig. 5A). This indicates that cell adhesion to the substrate
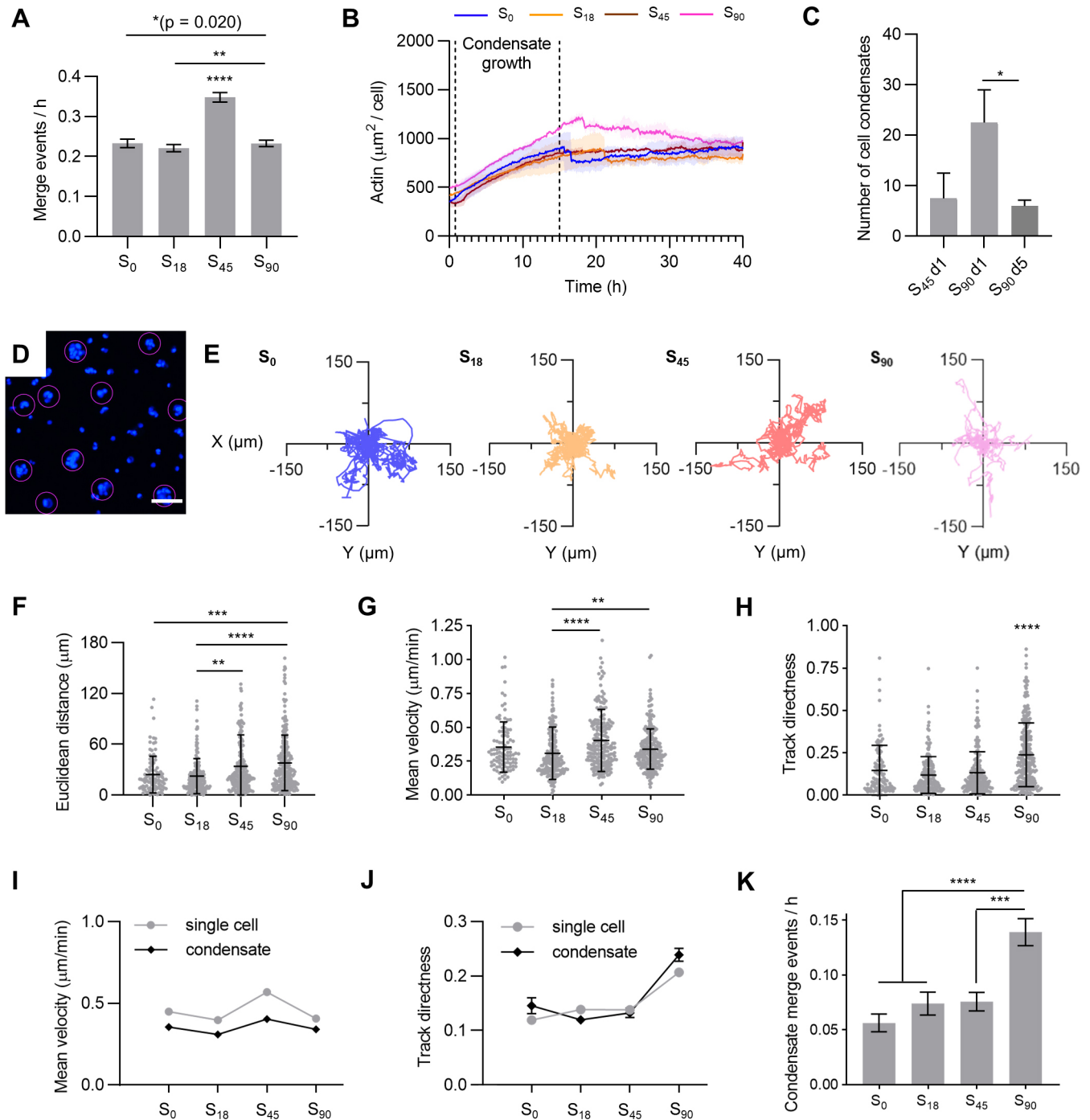
Fig. 4. Formation of mesenchymal cell condensates. (A) Quantification of the merge events per hour in cell tracks on the indicated substrates; $941 \leq n \geq 2183$ tracks. (B) Quantification of the spreading area during cell tracking, assayed using actin staining (SiR-actin), showing the region assigned to cell condensate growth (dashed lines). $n=9$ cells. Values from 48 min to 15 h have been fitted to a linear model, and the results are summarized in Table S1. (C) Quantification of the number of cell condensates per substrate on S_{90} and S_{45} nanopatterns formed after 1 day or 5 days of chondrogenic induction, as indicated; at least $n=2$ replicates per independent experiment. (D) Representative image of cell nuclei (blue) showing cell condensates segmented for tracking (contained in purple circles) at 20 h of imaging. Scale bar: 100 µm. (E) Migratory trajectories for cell condensates on the indicated substrates, $n=20$ trajectories. The beginning of each trajectory has been aligned at the origin of the Cartesian coordinate system. (F–H) Quantification of the Euclidean distance (F), mean velocity (G) and track directness (H) of cell condensates. $101 \leq n \leq 247$ tracks. (I,J) Comparison of mean velocity (I) and track directness (J) between single cells and cell condensates. $101 \leq n \leq 5177$ tracks. (K) Quantification of the merge events per hour in cell condensate tracking. $178 \leq n \leq 211$ tracks. Data in A–C and I–K are presented as mean±s.e.m. Data in F–H are presented as mean±s.d. Data are from at least two independent experiments, with all data from all experiments used in the calculations. Statistical significance was determined by a Kruskal–Wallis test with Dunn's multiple comparison post hoc test in A, F–H and K, and by an unpaired two-tailed Student's t-test in C. *$P<0.05$, **$P<0.01$, ***$P<0.001$, ****$P<0.0001$.

Single-cell
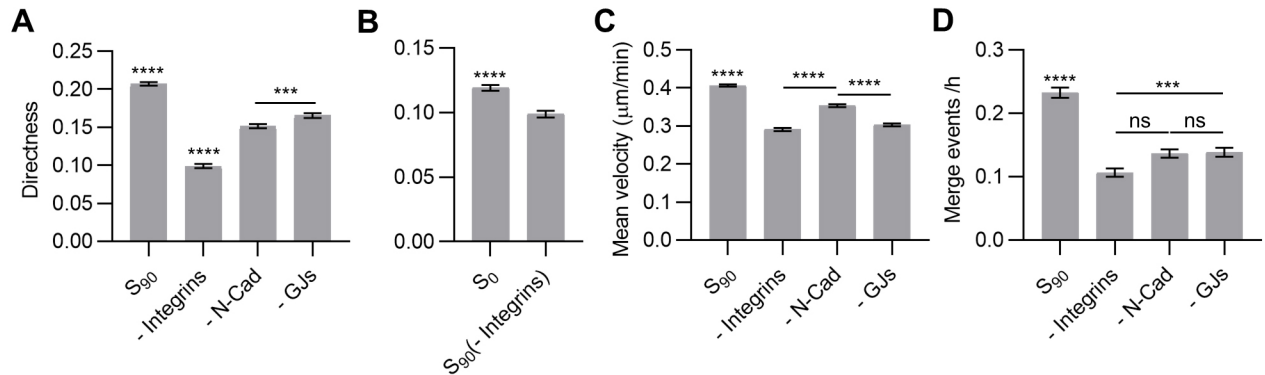
Condensate
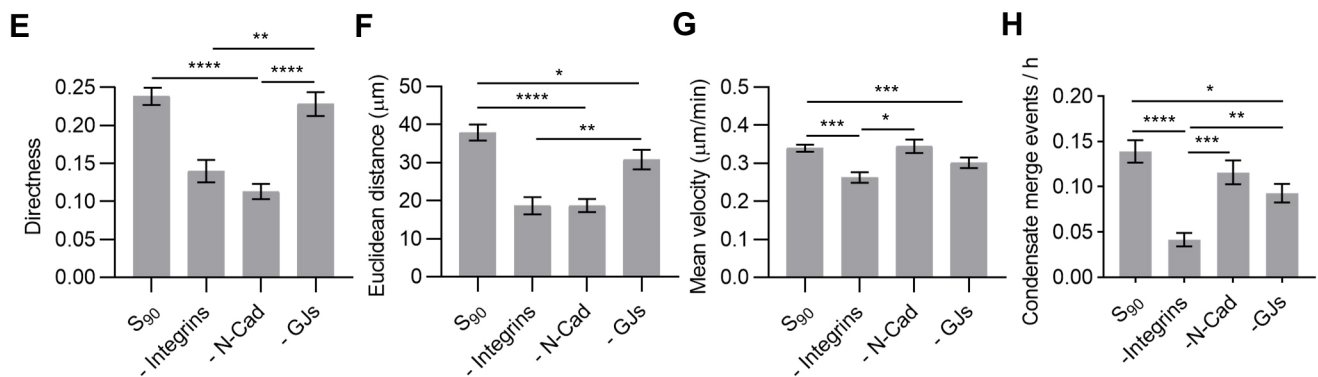
Fig. 5. Effects of pharmacological inhibitors on single-cell migration and collective cell migration on S_{90} nanopatterns. (A–D) Quantification of directness (A,B), mean velocity (C) and merge events per hour (D) in single-cell tracking. $1574 \leq n \leq 5177$ tracks. (E–H) Quantification of directness (E), Euclidean distance (F), mean velocity (G) and merge events per hour (H) in collective cell migration of cell condensates. $85 \leq n \leq 247$ tracks. Data are presented as the mean±s.e.m. Migration was assayed on S_{90} substrates without (S_{90}) or with the following pharmacological interventions: RGD dendrimers in solution (−Integrins), ADH1 (−N-Cad) or 18βGA (−GJs). In B, directness of single-cell migration on S_0 is shown for comparison. Data are from at least two independent experiments, with data from all experiments used in the calculations. Statistical significance was determined by a Kruskal–Wallis test with Dunn's multiple-comparison post hoc test. *$P<0.05$; **$P<0.01$; ***$P<0.001$; ****$P<0.0001$; ns, not significant.

is more relevant than cell–cell interactions in determining the directionality of single-cell migration. Moreover, the value of directness after treatment was even lower that the one measured on S_0 control substrates (Fig. 5B). Quantification of the mean cell velocity showed that all pharmacological treatments caused a significant, although small, reduction in the migration speed. Integrin blocking and the uncoupling of GJs by 18βGA had a similar effect (cells were ~25% slower), and ADH1 treatment to block N-Cad reduced the mean velocity of the cells by 13% (Fig. 5C). The merge events per hour were significantly reduced following all the treatments, especially upon integrin blockage. Both ADH1 and 18βGA treatments reduced the hourly rate of merge events between tracks by 40%, whereas integrin blocking induced a maximum reduction of 55% (Fig. 5D).

In the analysis of cell condensate migration, we observed that directionality was affected by integrin blockage, causing a 41% decrease in directness, and by N-Cad inhibition, which led to a 53% decrease in directness (Fig. 5E). However, GJ disassembly had a lesser effect on directional persistence, causing a small change in Euclidean distance (19% decrease) and having no significant effect on directness (Fig. 5E,F). Similar to the single-cell tracking results, quantification of the mean velocity in cell condensates (Fig. 5G) revealed that GJ disassembly and integrin blockage caused significant, but small, reductions in the migration rate (11% and

23% decrease, respectively), and no significant effects were observed upon N-Cad inhibition. The merge events between cell condensates were severely affected by integrin blockage, which caused a 3-fold decrease in their hourly rate, whereas the disassembly of GJs caused a 33% decrease, and N-Cad inhibition had no significant effects on the rate at which cell condensates merged (Fig. 5H).

DISCUSSION
Mesenchymal cell condensation is a fundamental step in chondrogenesis, producing cell condensates from which early cartilage structures grow and develop. The process encompasses a dynamic cell recruitment towards centers of condensation, in which the adhesive extracellular glycoprotein FN is upregulated. Despite the relevance of this process both *in vivo* and *in vitro*, the mechanisms of chondrogenic condensation have been largely overlooked. It has been proposed that condensation results from directional migration of cells from the surrounding loose mesenchyme to regions of increased matrix adhesion, where cells adopt a close-packed configuration and acquire epithelioid characteristics. Here, we studied hASC migration during mesenchymal cell condensation under chondrogenic stimuli by live-cell imaging, as well as the dependence of hASC migration on the matrix adherence. With this aim, we used nanopatterned substrates previously developed in our group that

allow control of the local surface adherence. These substrates have been proved to sustain cell culture and chondrogenic differentiation *in vitro* (Casanellas et al., 2020; Lagunas et al., 2017).

Cells cultured on the substrates showed a range of traits that transitioned from more amoeboid to more mesenchymal with increasing substrate adhesiveness. Cells on the S_{FN} control substrate spread quickly after seeding, displaying a typical mesenchymal migration with spindle-like elongated morphologies and exerting traction forces against the substrate through FAs associated with actin-rich protrusions. Cell migration on S_{FN} was the slowest of all the analyzed conditions, which is in agreement with previous reports indicating that the velocity of amoeboid migration is usually higher than that of mesenchymal migration (Paňková et al., 2010; Ruprecht et al., 2015).

Conversely, cells on the S_0 substrate and on the nanopatterns exhibited amoeboid-like migration with rounded irregular cell morphologies, and transient expansion and contraction cycles with protruding filopodia. They exhibited a cortical actin organization that concentrated at the rear part of the cell during migration, which has previously been reported to be a consequence of localized retrograde flow that is generated by active actin polymerization in the filopodia and that pushes the cortex backwards (Liu et al., 2015; Renkawitz et al., 2009). Amoeboid migration is generally observed in cells migrating on low-adherence substrates under spatial constraints, such as in microfluidic devices or hydrogels (Liu et al., 2015). This mode of migration has been recently reported in cancer and epithelial cells migrating freely on soft, viscoelastic substrates (Adebowale et al., 2021), as well as neural progenitors cultured at low density (Kawaguchi et al., 2017).

Cells can switch between migration modes depending on the context (Yamada and Sixt, 2019). Migration plasticity between mesenchymal and amoeboid migration has been extensively studied in cancer dissemination, where it is termed mesenchymal-to-amoeboid transition (MAT). MAT endows mesenchymal cells with amoeboid features that facilitate migration through complex 3D environments, aiding cancer metastasis (Graziani et al., 2022). The switching between migration modes has been related to three key parameters: protrusion, contractility and adhesion (Lämmermann and Sixt, 2009), and the transition to fast amoeboid-like migration has been described under conditions of low adhesion and strong confinement (Liu et al., 2015). Here, we observed that hASCs under chondrogenic induction adapted their migration mode to the substrate adhesiveness, influencing both single-cell and collective migration during cell condensation.

Significantly longer protrusions were generated by cells on S_{90} nanopatterns, indicating that they are sensitive to the RGD integrin-ligand density. Although no FAs were present on the amoeboid-like hASCs, amoeboid cells migrating on 2D substrates require surface receptors to adhere to the substrate, preventing Brownian motion from separating surface contacts, and to sustain actin retrograde flow during migration. We observed that β1 integrins were homogeneously distributed on the plasma membrane of the cells, as has been described previously for amoeboid T lymphocytes (Friedl et al., 1998). These diffusively distributed anchor points have been found to be sufficient to generate the traction forces necessary for the migration of low-adhesive cells (Graziani et al., 2022; Lämmermann and Sixt, 2009).

Quantification of the mean velocity from cell tracking showed that cells migrated significantly faster on mid-adherence substrates (S_{45}), which is in agreement with previous studies demonstrating a biphasic dependence of cell migration velocity on cell–substrate adhesiveness, where maximum speed is reached at intermediate

levels of adherence (DiMilla et al., 1993). Cell migration based on anchoring receptors requires dynamic building and breakage of attachments to the substrate. On low adherent substrates (S_0 and S_{18}), the scarceness of anchor points compromises traction force during migration, whereas with the increasing substrate adherence, transient contacts become more stable, enhancing traction force but also making rearward detachment more difficult. A balance between these two situations is given by S_{45} nanopatterns, thus inducing a peak in the migration rate.

We examined three different indicators of directional persistence: directness, turning angle and MSD. MSD contains information about both speed and directional persistence and is a good measure of the surface area explored by the cells over time. We found that higher substrate adhesiveness made the cell movement more directional. Directional persistence in cell motility relies on preserving the established front–rear polarity upon cell symmetry breaking (Hennig et al., 2020). The increasing availability of adhesion sites (higher adhesiveness) could minimize turning and thus favor persistence; however, at the same time, it might introduce conflicting directional signals. Sung et al. have demonstrated that the autocrine secretion of exosomes from late endosomes is required for directionally persistent cell movement of migrating cancer cells *in vivo* and *in vitro* (Sung et al., 2015). Exosome secretion precedes and promotes adhesion assembly at the leading edge, stabilizing nascent protrusions, which become larger and long-lived. *In vitro* experiments have shown that FN from serum or from surface coatings is targeted to exosomes by binding to cognate cellular integrin receptors and is then secreted in adhesive form to promote adhesion formation (Sung et al., 2015). Although most probably also aided by other signaling cargoes (Luga et al., 2012), adhesive ligand availability (either RGD or FN) on our most adherent substrates (S_{90} and S_{FN}, respectively) might favor adhesion recycling, exosome formation and trafficking, thereby promoting polarization maintenance and directionality. However, the abrupt increase of directionality observed for cells on S_{FN} substrates (2-fold increase in directness compared to that of cells on S_{90}) cannot be explained in terms of ligand density alone, as S_{90} and S_{FN} substrates have only a relatively small difference in the percentage area covered with RGD groups at inter-dendrimer distances of less than 70 nm: from 90% for S_{90} to presumably 100% for S_{FN}, given a molecule size of 15.5×8.8 nm (Koteliansky et al., 1980). However, the spatial positioning of RGD groups on native FN would differ from that of nanopatterned RGD dendrimers, generating different sets of cell–substrate interactions and differently affecting cell adhesion and migration (Cavalcanti-Adam et al., 2007). Moreover, integrin binding to FN is also modulated by synergy sites in the FN protein, which are absent in isolated RGD dendrimers (Brown et al., 2015). Finally, a coating of whole FN protein does not engage all the same integrin types that isolated RGD motifs do (Humphries et al., 2006; Moreno-Layseca et al., 2019), which can also contribute to a difference in cell behavior if the activated integrins have different parallel biological functions (Elosegui-Artola et al., 2014).

Our results point to the importance of directionality, rather than speed, in determining how far a cell will migrate. Although moving at greater speed allowed cells on S_{45} substrates to cover a longer sum trajectory, their lack of directionality meant that the Euclidean distance migrated remained lower than that of cells on S_{90} or S_{FN} (Fig. S5). On the other hand, moving in straighter paths allowed cells on S_{FN} to migrate further and explore larger surface areas, as demonstrated by MSD measurements, even though they migrated with a lower velocity than cells in all other conditions. Tellingly, cells on S_0, S_{18} and S_{90} substrates had very similar mean velocities

(lower than that of cells on S_{45}); nevertheless, a more directed movement also allowed cells to migrate slightly further on the S_{90} substrate than on the S_0, S_{18} or S_{45} substrates.

To account for cell–substrate interactions, we performed a whole-cell simulation of cell migration by adapting the model developed previously by Odde and co-workers (Chan and Odde, 2008). Calculation of RMCs revealed a biphasic dependence on adhesion, as previously reported (Klank et al., 2017), with peak RMC values observed for cells on the S_{45} substrate, effectively reproducing the experimental data. However, we found discrepancies between empirical and simulated MSD curves, which we attributed to variation in the directional persistence of cells on the different substrates. Indeed, deviations from the PRW model have been reported, especially at large time intervals (Dickinson and Tranquillo, 1993; Dieterich et al., 2008). Alternatively, other mechanisms affecting MSD have been proposed, such as the zig-zagging observed in the motile amoeba *Dictyostelium discoideum*, which aids maintenance of directional persistence during cell movement (Li et al., 2008).

Chondrogenic cell culture medium induces cell aggregation on the nanopatterned substrates, resulting in formation of cell condensates (Lagunas et al., 2017). During condensation, cells gather and establish intimate cell–cell contacts, for which migrating cells need to collide and become engaged. To evaluate cell condensate formation, we first quantified the rate of merge events as the instances of two tracks reaching a spacing of less than 30 μm between the nuclei of migrating cells, at which point we assume cell–cell contact is established. We found that the probability of cell–cell encounters is higher for the fastest migrating cells (those on S_{45} nanopatterns). It should be noted that condensation involves not only merging, but also splitting events in which cells that established transient adhesions come apart. In live-cell imaging experiments, we observed that single cells sometimes probe a condensate and join it for only a few minutes before exiting; other times, a cell is pulled from a condensate by those in another one nearby. Hence, while the rate of merge events does not directly correlate with the number of cells present in the final constructs, it reveals that cell migration on the S_{45} substrate is a more dynamic system, in which cells come into contact more often than those on other substrates. However, although more frequent, cell–cell collisions on S_{45} led to fewer condensations than on S_{90} nanopatterns.

Cell–cell engagement during migration is restricted by the occurrence of CIL. CIL is a process through which a cell ceases motility or changes its trajectory upon collision with another cell. CIL was first proposed by Abercrombie and Heaysman, who observed that cells exhibiting CIL do not crawl over each other (Abercrombie and Heaysman, 1954). As suggested previously, CIL-mediated repulsion is expected to be reduced or switched off during mesenchymal cell condensation in chondrogenesis to facilitate cell–cell interactions (Stramer and Mayor, 2017). In neural crest cells, cell–matrix adhesions are disassembled near the cell–cell contact immediately after collision, which generates the tension across the cell contact needed to induce separation during CIL (Roycroft et al., 2018). As fewer cell–substrate adhesions are built on S_{45} than on S_{90} (due to fewer anchor points being available), we assume that their disassembly at the cell–cell contact would be energetically more favorable, thus promoting CIL and preventing condensation. Conversely, inhibition of CIL-mediated repulsion results in an increase in the length, area and stability of cell–matrix adhesions together with a change in actin organization that results in formation of stress fibers near the contact (Roycroft et al., 2018). This could explain the observation of Pax-rich FAs on those cells already

forming cell condensates on S_0 substrates and on the nanopatterns. The disassembly of cell–matrix adhesions at the cell–cell contact is reported to be mediated by focal adhesion kinase (FAK, also known as PTK2)–proto-oncogene tyrosine-protein kinase Src (hereafter referred to as Src) signaling that works downstream of N-Cad. Upon contact, cells establish a functional N-Cad-based adhesion that activates Src. Src, through FAK, promotes the disassembly of cell–matrix adhesions at the cell–cell contact, reducing traction and increasing tension, which is required for cell separation during CIL (Roycroft et al., 2018).

Mesenchymal collective migration is characterized by the cooperative interaction of groups of cells that can be connected through either transient or stable cell–cell contacts, depending on cell density (Theveneau and Mayor, 2013). We analyzed the migration dynamics of condensates on the nanopatterned substrates, and we found that substrate adhesiveness has comparable effects on collective cell migration and on single cells. Similar migration behaviors in individual and collective groups of migrating cells have been previously reported. Mesodermal cells isolated from the migrating cohort are able to migrate independently and in a similar way to the whole group (Arboleda-Estudillo et al., 2010; Ulrich et al., 2005), and in a more recent study, mouse cancer cells forming multicellular spheroids on 2D substrates have been found to follow the same migration modes as single cells (Beaune et al., 2018). Our results show that the rate of migration was similarly reduced for cell condensates on all the different substrates when compared to the rate of single-cell migration, thus indicating that cell condensates are slower than single cells independently of the substrate adherence. We also observed that the directionality of the movement was preserved from single cells to cell condensates on the same substrates. As in single-cell migration, cell condensates must distinguish a front and a rear to migrate directionally and maintain a certain degree of cohesiveness among the cell cohort to coordinate the movement. As in other models of mesenchymal collective migration (Scarpa and Mayor, 2016), we observed that the whole cell condensate is migratory, with cells rapidly exchanging positions and forming large lamellipodial protrusions in the direction of migration at the edge of the condensate (Movie 11). These protrusions, in analogy to single migrating cells, exert traction forces against the ECM to allow collective cell movement. As observed in *Xenopus* mesendoderm cells and neural crest cells, integrin–FN interactions are required for migration and deployment into the tissue (Alfandari et al., 2003; Boucaut and Darribere, 1983). The inhibition of α5β1 integrin impairs mesendoderm migration and protrusion formation (Davidson et al., 2002). This agrees with our observation that integrin blockage has a major impact on the migration of both single cells and mesenchymal cell condensates on S_{90} nanopatterns, especially affecting the directionality of the movement, which reaches values below those observed for cells on S_0 control substrates. Indeed, during mesenchymal development, cell–substrate interactions become progressively more relevant in an environment in which the matrix becomes denser over time (Kalson et al., 2015; Singh and Schwarzbauer, 2012).

Alongside cell–substrate interactions, cell–cell adhesions and cell communication have been shown to modulate the migration speed and directionality of collectively migrating mesenchymal cells. N-Cad is the main adherens junction protein, mediating cell–cell interactions during mesenchymal cell condensation, and previous studies have shown that the expression of mutant forms of N-Cad lacking either the extracellular homotypic interaction domains or the intracellular β-catenin binding site results in impaired condensation

and chondrogenesis (DeLise and Tuan, 2002; Oberlender and Tuan, 1994). Knockdown of N-Cad in bone marrow-derived mesenchymal stem cells compromises migration in response to TGF-β from breast tumor (Choi et al., 2021), and N-Cad inhibition decreases colony spreading and average spreading velocities in a bladder cancer cell line (Zisis et al., 2022). Accordingly, we found that blocking N-Cad with ADH1 reduced the mean velocity of single cells on S_{90} nanopatterns. These results are consistent with single-cell migration within a multicellular setting being mediated by the transient contacts that occur between mesenchymal cells (Theveneau and Mayor, 2012). Strikingly, although no significant effects on the velocity of cell condensates were found upon inhibition of N-Cad, the directness was decreased to a level similar to that seen after integrin blockage. This magnification of the effects of N-Cad on the directionality of movement in cell condensates can be attributed to its role in maintaining group cohesiveness during migration.

Mesenchymal cell condensation proceeds with the formation of a widespread GJ communication network that allows cell synchronization and mediates the coordination within multicellular groups towards the formation of tissue (Coelho and Kosher, 1991; Mayan et al., 2015). Connexin 43 (Cx43, also known as GJA1)-based GJs are essential in chondrocyte differentiation, and Cx43 deficiency leads to skeletal defects (Gago-Fuentes et al., 2016). We found that uncoupling of GJs using 18βGA caused a reduction in the directness and mean velocity of single cells migrating on S_{90} nanopatterns. This is consistent with previous single-cell tracking data of mesenchymal cells from elongating feather bud of chicken dorsal skin explants. In that study, the authors found that electrical coupling via GJs mediates the conversion of sporadic Ca^{2+} transients into organized oscillations that facilitate collective mesenchymal cell migration during feather elongation in the posterior–distal direction. Treatment with the inhibitor carbenoxolone (an 18αGA derivative) was found to alter cell movement, especially the directionality (Li et al., 2018). We found that 18βGA treatment of migrating mesenchymal cell condensates on S_{90} nanopatterns caused a slight decrease in the migration rate and surprisingly, no significant effects on directness. Li et al. (2018) have suggested that the mechanism they described involving GJs in the collective mesenchymal migration in feather elongation is active in transient cell collectives to aid them to coordinate during the formation of organ architectures, and this mechanism might not be required in more stable adhesion-molecule-mediated cell condensates.

Although merge events in single-cell migration seemed to be dictated by the mean velocity, with cells on S_{45} substrates showing the highest migration rate and producing the highest number of hourly merge events, the dramatic impact of the pharmacological interventions on the merge events per hour observed for cells on S_{90} nanopatterns, which showed a major decrease in directness compared to the change in migration rate after treatment, suggested that the directionality of the movement has a non-negligible effect on cell–cell collisions. Importantly, the merging events per hour for cell condensates were found to be significantly higher on S_{90} substrates, where the groups of cells moved more directionally.

We have shown previously that mesenchymal cell condensates produced on S_{90} nanopatterns are mechanically more stable than those produced on the other substrates, preserving the 3D configuration for up to 14 days in culture, and are the only ones able to enter the early stages of the chondrogenic pathway, which occurs after 6 days of chondrogenic induction (Casanellas et al., 2020, 2022; Lagunas et al., 2017). To avoid hypertrophy as the most probable final outcome for mesenchymal stem cells stimulated

towards chondrogenesis, current regenerative medicine approaches focus on controlling the primary stages of chondrogenic commitment to favor the formation of hyaline cartilage (Chen et al., 2015). In that sense, it seems a natural approach to tackle substrate adhesions during cell gathering and condensate formation as one of the first steps in cartilage development. Here, we show that substrate adhesions have a dramatic effect in both single-cell and collective migration of condensates. Single cells migrating on S_{90} nanopatterns present characteristics that can be considered as intermediate between amoeboid and mesenchymal migration, which favor both cell gathering and condensation. Cells show increased directionality and reduced CIL, allowing them to condensate but at the same time providing a sufficiently dynamic framework in which there is a balance between cell–substrate and cell–cell adhesions for condensates to grow. Therefore, we envision that the results obtained could have an immediate application in cartilage regeneration strategies and could also be applied to the study of other biological processes involving transitions between mesenchymal and amoeboid migration modes, such as cancer progression.

MATERIALS AND METHODS
Preparation of poly(L-lactic acid)-coated substrates
Nanopatterned substrates were prepared as previously described (Casanellas et al., 2018; Lagunas et al., 2017). Corning glass microscopy slides (Sigma-Aldrich, Madrid, Spain) were cut with a diamond-tip cutter to square pieces of 1.25×1.25 cm. Slides were washed thoroughly with deionized water (18 MΩ cm, Milli-Q; Millipore, Madrid, Spain) followed by 96% ethanol and were then air-dried. A 2% (m/v) solution of 95/5 L-lactide/D,L-lactide copolymer (PLLA; Corbion, Barcelona, Spain) was prepared by adding 200 mg of solid polymer to 10 ml of 1,4-dioxane (Sigma-Aldrich, 296309; Madrid, Spain) in a pressure tube with a magnetic stirring bar. The tube was placed in a silicon oil (Thermo Fisher Scientific, 174665000; Barcelona, Spain) bath on a hotplate at 60°C with gentle stirring (300 rpm) overnight, and the solution was transferred to a 15 ml vial for storage at room temperature. Glass substrates were spin-coated with the PLLA solution in a class 10,000 clean room. Slides were placed on a hotplate at 60°C for at least 10 min to dry. Each slide was fixed on the spin-coater with vacuum, and 200–250 μl of PLLA solution was added using a Pasteur pipette, covering the whole surface. Slides were coated in a two-step program: 5 s at 500 rpm with an acceleration of 300 rpm s^{-1} (to eliminate excess solution and spread the remaining solution homogeneously on the surface) followed by 30 s at 3000 rpm with an acceleration of 1500 rpm s^{-1}.

Nanopatterning of RGD-Cys-D1 dendrimers on substrates
All steps were performed in a sterile tissue culture hood, and only sterile materials, solutions and techniques were used. Spin-coated PLLA substrates were treated for 13 min under UV light. Deionized water was used to prepare RGD-functionalized dendrimer solutions. A stock solution was prepared by dissolving the solid dendrimer (Lagunas et al., 2014) in water; an intermediate solution and three working solutions were prepared from it. Dendrimer solutions were filtered through a 0.22 μm Millex RB sterile syringe filter (Merck Millipore, Madrid, Spain) attached to a syringe and then applied directly on the substrates. Substrates were left at room temperature overnight (16 h). Solutions were removed with a pipette in a cell-culture hood. Substrates were washed with sterile deionized water and left to dry on air. FN-coated substrates (S_{FN}) were produced by incubating PLLA substrates in FN from bovine plasma solution (Sigma-Aldrich, F1141; Madrid, Spain) at 100 μg ml^{-1} in phosphate-buffered saline (PBS; 21600-10, Gibco; Barcelona, Spain) for 1 h at room temperature, followed by washing with PBS, just before cell seeding.

Cell culture
Human adipose-derived mesenchymal stem cells (hASCs; PCS-500-011; ATCC, VA, USA) were cultured in T75 flasks at 37°C and 5% CO_2 in

growth medium, which consisted of Mesenchymal Stem Cell Basal Medium (PCS-500-030; ATCC, VA, USA) supplemented with Mesenchymal Stem Cell Growth Kit Low Serum (PCS-500-040; ATCC, VA, USA) and 0.1% (v/v) penicillin-streptomycin (P/S; 15140; Invitrogen, Barcelona, Spain). Medium was replaced every 2–3 days. Passaging was carried out when cells reached 70–80% confluence.

Live-cell imaging
Prior to imaging, hASCs at passage 3–4 were incubated in growth medium with SiR-actin (Tebu-bio, SC001; Barcelona, Spain) at 200 nM for 4 h, or 750 nM for 1.5 h. Cells were then incubated in medium with Hoechst 33342 (1:1000; Invitrogen, H3570; Barcelona, Spain) for 5 min. Cells were trypsinized and seeded on the substrate at a density of 30,000 cells/cm^2 in a glass-bottom microscopy dish (VWR, 734-2906H; Barcelona, Spain) in chondrogenesis-inducing medium (PCS-500-051; ATCC, VA, USA) with 100 nM SiR-actin. The sample was immediately transferred to the microscope stage, which was pre-conditioned to 37°C and 5% CO$_2$. Live-cell imaging was performed using a Nikon Eclipse Ti2-E inverted microscope with a Prime 95B sCMOS camera (Photometrics, Birmingham, UK) and an Okolab Cage Incubator (Okolab, Pozzuoli, Italy), with a 10× objective. Samples were imaged for 40 h. Images were taken every 6 min for the phase-contrast, blue and far-red (Cy5) channels. At least two samples of each condition were imaged and analyzed.

Single and collective cell segmentation and tracking
Live-cell imaging stacks of Hoechst 33342-stained samples were analyzed for cell movement. The first 17 frames (96 min) were removed to omit drifting prior to cell adhesion. Cell nuclei were tracked with the TrackMate plugin in ImageJ (ImageJ version 2.0.0; NIH, MD, USA). Nuclei were segmented with the Laplacian of Gaussian (LoG) detector, setting an estimated blob diameter of 15 µm and a threshold of 4 µm. No further filters were applied. The LAP Tracker was used with a maximum frame-to-frame linking distance of 50 µm and allowing gap closing to a maximum of 50 µm over 1 frame. For analysis, frame depth was not limited.

Analysis of collective cell migration in multicellular condensates was performed on the second half (20–40 h) of live-cell imaging, using Hoechst 33342-stained stacks, as described above for single cells except for the following parameters: condensates were segmented with an estimated blob diameter of 70 µm and a threshold of 40 µm, and gap closing was allowed over 3 frames. All subsequent steps in track analysis were performed in the same way for single cells and condensates.

Track analysis
Tracks with duration under 3 h were excluded to avoid skewed results due to artificially short tracks. However, analysis of all available tracks rendered highly similar results (data not shown).

Track net displacement and duration were extracted from the Track Statistics output file of TrackMate. Sum trajectory was calculated using R Studio (R Studio version 4.0.2, MA, USA) from the Links Statistics output file by adding the displacements of all links in each track. Mean track velocity was calculated by dividing track trajectory (in µm) by track duration (in minutes).

To analyze track directionality, directness was first obtained as the ratio between the net displacement (Euclidean distance) and the sum trajectory of each track. Turning angles were calculated using Microsoft Excel from the Spots Statistics output of TrackMate. Vector components were found by subtracting particle coordinates at the start of each 6-min link from those at the start of the next one (two consecutive spots) within each track. The angles between pairs of consecutive vectors were then found using the following equation, where u and v are the two vectors, and α is the angle between them:

$$\alpha = \cos^{-1}\left(\frac{u \times v}{\|u\| \times \|v\|}\right).$$

Angles with values equal to 0 or 180 were excluded to account for static cells and single-link tracks. Angles were categorized into 15-degree sections according to their value, and section percentages were calculated and plotted in polar histograms using the Plotly package in R Studio (R Studio version 4.0.2, MA, USA).

The number of merge events per track was obtained by running a second TrackMate analysis with the settings as above but allowing track merging when nuclei collided at a distance under 30 µm (for single-cell migration) or under 120 µm (for multicellular condensates). The number of merge events per track was divided by the duration to obtain an hourly rate of merge events.

Actin staining and spreading analysis
Actin was stained in live-cell imaging experiments using SiR-actin. A threshold was applied to select for the actin staining area, which was defined as the area with pixel intensity values from ∼117 (manually adjusted according to staining intensity in each live-cell imaging file) to 255. Actin staining area in each frame was automatically measured with the Analyze Particles tool in ImageJ (ImageJ version 2.0.0, MD, USA), selecting for particles above 10 µm^2.

The number of nuclei or condensates in each frame was measured using the Hoechst 33342 staining signal. An automatic threshold was applied, and particles of 3–3000 µm^2 were counted in each frame using the Analyze Particles tool. Total actin area was then normalized to nuclei or condensate number in each frame to obtain the area of cell spreading over time. Actin data from 48 min to 15 h of imaging were fitted to a linear model using R Studio (R Studio version 4.0.2, MA, USA).

Immunostaining
Cells were carefully rinsed with PBS, fixed with formalin solution (Sigma-Aldrich, HT5011; Madrid, Spain) for 20 min at room temperature, and rinsed again twice with PBS. Aldehyde groups were blocked with 50 mM ammonium chloride (Sigma-Aldrich, A9434; Madrid, Spain) in PBS for 20 min. Samples were permeabilized using saponin (Sigma-Aldrich, 47036; Madrid, Spain) at 0.1% (m/v) in blocking solution [1% (m/v) bovine serum albumin (BSA; Sigma-Aldrich, A3059; Madrid, Spain) in PBS] for 10 min. Cells were washed with PBS and incubated with a mouse monoclonal [12G10] anti-human integrin β1 antibody at 8 µg ml^{-1} (Abcam, ab30394; Cambridge, UK), and with a rabbit monoclonal [Y113] anti-human Pax antibody at 5 µg ml^{-1} (Abcam, ab32084; Cambridge, UK), overnight at 4°C in blocking solution. Afterwards, cells were washed with PBS and treated with the following fluorophore-conjugated secondary antibodies: Alexa Fluor 568-conjugated anti-rabbit IgG (Life Technologies, A11036; Thermo Fisher Scientific, Barcelona, Spain) and Alexa Fluor 488-conjugated anti-mouse Ig (Life Technologies, A10667; Thermo Fisher Scientific, Barcelona, Spain). Secondary antibodies were used at 1 µg ml^{-1} in blocking solution for 1 h at room temperature, covered from light. Samples were washed with PBS and left to dry on air for 5–10 min, then placed on a Corning 7.5×2.5 cm microscopy slide. One drop (50 µl) of Fluoromount mounting medium (Sigma-Aldrich, HT5011; Madrid, Spain) was added, and a Corning 1.8×1.8 cm coverslip (Sigma-Aldrich, 2845-18; Madrid, Spain) was placed on the sample, avoiding the formation of bubbles. Mounted samples were stored at 4°C covered from light, and images were taken using a Leica SPE upright confocal microscope (Leica Microsystems, Wetzlar, Germany) and processed using Fiji (https://fiji.sc/).

Measurement of filopodia
Filopodia were measured from phase-contrast images taken at 8 h of live-cell imaging. Images were assessed for any visible filopodia, which were manually measured along their longitudinal axis using ImageJ (ImageJ version 2.0.0, MD, USA).

Calculation of MSD
We calculated the MSD from the experimentally obtained cell trajectories using a modified version of the @msdanalyzer tool (https://github.com/tinevez/msdanalyzer; Tarantino et al., 2014) written for MATLAB

(MATLAB R2016a; MathWorks, MA, USA), using the following equation:

$$MSD_i(\tau) = \sum_t (r_i(t+\tau) - r_i(t))^2,$$

where τ is the delay, t is the time and r_i is the distance.

To run the code, the cell array containing the time and cell coordinates was imported into a MATLAB array. To initialize the analyzer, units should be provided for the time and space measurements. Details of the code used to establish the array, calculate MSD, create plots and recover data are available from the authors upon reasonable request.

Calculation of MSD and RMC from a stochastic whole-cell model

MSD was obtained as an output of the simulation conducted using the 2D whole-cell model for cell migration developed by Odde and co-workers (Chan and Odde, 2008; Bangasser et al., 2013; Klank et al., 2017). It was calculated from the coordinates of the simulated cell center over a time interval. The displacement of the cell during a known time interval d(t) is related to the averaged speed S and the directional persistence time P, and thereby the MSD can be written as follows:

$$MSD(t) = 2S^2P[t - P(1 - e^{-t/P})].$$

For $t \gg P$, MSD is linearly dependent on t with a slope $2S^2P$. As a measure of cell dispersion over long periods of time, and analogous to a diffusion coefficient, the RMC can be defined from this limiting slope as follows:

$$RMC = \lim_{t \to \infty} \frac{MSD(t)}{2n_d t} = \frac{1}{n_d} S^2,$$

where n_d is the number of dimensions; $n_d=2$ for a planar substrate. In the simulation, this was calculated by fitting the MSD curve using a nonlinear least-squares regression analysis that accounts for unequally distributed and correlated residuals, as has been previously described (Dickinson and Tranquillo, 1993).

Blocking of cell–substrate and cell–cell interactions

For integrin blocking, RGD-Cys-D1 dendrimers were added to the medium to a final concentration of $4 \times 10^{-9}\%$ (w/w). We selected this dendrimer concentration because it yields S_{18} substrates. During substrate functionalization, equilibrium is reached between dendrimer concentration in solution and adsorbed dendrimer density; hence, use of the concentration corresponding to the substrates with the lowest density prevents further adsorption mid-assay. Thus, additional dendrimers will not adsorb on the S_{90} substrate but rather attach to free integrin receptors, blocking their interactions with dendrimers on the surface.

To block N-Cad and induce GJ disassembly, 300 µM ADH1 or 20 µM 18βGA, respectively, were added to the chondrogenic medium at the start of imaging. We selected those concentrations based on available literature (Erez et al., 2004; Madl et al., 2017; Madl et al., 2019; Shintani et al., 2008; Williams et al., 2000; Böhmer et al., 2001; Guan et al., 1996) and after observing lesser effects at lower doses but significant cell death at higher doses (1000 µM for ADH1, 120 µM for 18βGA).

Statistics

Quantitative data are displayed showing the mean and s.d. or s.e.m., as indicated for each panel. n is the sample size (i.e. the number of tracks analyzed). All experiments were performed at least twice ($N=2$), with all data from both computed in the calculations. Data were subjected to a Kolmogorov–Smirnov normality test. For data following a normal distribution, significant differences were judged using an unpaired two-tailed Student's t-test when only two groups were compared. Where data did not pass a normality test, a Kruskal–Wallis test with Dunn's test for multiple comparisons was applied. Statistics were performed using OriginPro 8.5 (OriginLab, Madrid, Spain) and GraphPad Prism 8.3 (GraphPad Software, CA, USA).

References
Abercrombie, M. and Heaysman, J. E. M. (1954). Observations on the social behaviour of cells in tissue culture II. "Monolayering" of fibroblasts. *Exp. Cell Res.* **6**, 293-306. doi:10.1016/0014-4827(54)90176-7

Adebowale, K., Gong, Z., Hou, J. C., Wisdom, K. M., Garbett, D., Lee, H.-P., Nam, S., Meyer, T., Odde, D. J., Shenoy, V. B. et al. (2021). Enhanced substrate stress relaxation promotes filopodia-mediated cell migration. *Nat. Mater.* **20**, 1290-1299. doi:10.1038/s41563-021-00981-w

Alfandari, D., Cousin, H., Gaultier, A., Hoffstrom, B. G. and Desimone, D. W. (2003). Integrin α5β1 supports the migration of Xenopus cranial neural crest on fibronectin. *Dev. Biol.* **260**, 449-464. doi:10.1016/S0012-1606(03)00277-X

Arboleda-Estudillo, Y., Krieg, M., Stühmer, J., Licata, N., Muller, D. and Heisenberg, C. (2010). Movement directionality in collective migration of germ layer progenitors. *Curr. Biol.* **20**, 161-169. doi:10.1016/j.cub.2009.11.036

Arnold, M., Cavalcanti-Adam, E. A., Glass, R., Blümmel, J., Eck, W., Kantlehner, M., Kessler, H. and Spatz, J. P. (2004). Activation of integrin function by nanopatterned adhesive interfaces. *Chemphyschem* **5**, 383-388. doi:10.1002/cphc.200301014

Atchley, W. R. and Hall, B. K. (1991). A model for development and evolution of complex morphological structures. *Biol. Rev.* **66**, 101-157. doi:10.1111/j.1469-185X.1991.tb01138.x

Bangasser, B. L., Rosenfeld, S. S. and Odde, D. J. (2013). Determinants of maximal force transmission in a motor-clutch model of cell traction in a compliant microenvironment. *Biophys. J.* **105**, 581-592. doi:10.1016/j.bpj.2013.06.027

Beaune, G., Blanch-Mercader, C., Douezan, S., Dumond, J., Gonzalez-Rodriguez, D., Cuvelier, D., Ondarçuhu, T., Sens, P., Dufour, S., Murrell, M. P. et al. (2018). Spontaneous migration of cellular aggregates from giant keratocytes to running spheroids. *Proc. Natl. Acad. Sci. USA* **115**, 12926-12931. doi:10.1073/pnas.1811348115

Böhmer, C., Kirschner, U. and Wehner, F. (2001). 18-β-Glycyrrhetinic Acid (BGA) as an electrical uncoupler for intracellular recordings in confluent monolayer cultures. *Eur. J. Physiol.* **442**, 688-692. doi:10.1007/s004240100588

Boucaut, J. C. and Darribere, T. (1983). Fibronectin in early amphibian embryos. Migrating mesodermal cells contact fibronectin established prior to gastrulation. *Cell Tissue Res.* **234**, 135-145. doi:10.1007/BF00217407

Brown, A. C., Dysart, M. M., Clarke, K. C., Stabenfeldt, S. E. and Barker, T. H. (2015). Integrin α3β1 binding to fibronectin is dependent on the ninth type III repeat. *J. Biol. Chem.* **290**, 25534-25547. doi:10.1074/jbc.M115.656702

Casanellas, I., Lagunas, A., Tsintzou, I., Vida, Y., Collado, D., Pérez-Inestrosa, E., Rodríguez-Pereira, C., Magalhaes, J., Gorostiza, P., Andrades, J. A. et al. (2018). Dendrimer-based uneven nanopatterns to locally control surface adhesiveness: a method to direct chondrogenic differentiation. *J. Vis. Exp.* **131**, e56347. doi:10.3791/56347

Casanellas, I., Lagunas, A., Vida, Y., Pérez-Inestrosa, E., Andrades, J. A., Becerra, J. and Samitier, J. (2020). The Janus role of adhesion in chondrogenesis. *Int. J. Mol. Sci.* **21**, 5269. doi:10.3390/ijms21155269

Casanellas, I., Lagunas, A., Vida, Y., Pérez-Inestrosa, E., Rodríguez-Pereira, C., Magalhaes, J., Andrades, J. A., Becerra, J. and Samitier, J. (2022). Nanoscale ligand density modulates gap junction intercellular communication of cell condensates during chondrogenesis. *Nanomedicine* **17**, 775-791. doi:10.2217/nnm-2021-0399

Cavalcanti-Adam, E. A., Volberg, T., Micoulet, A., Kessler, H., Geiger, B. and Spatz, J. P. (2007). Cell spreading and focal adhesion dynamics are regulated by spacing of integrin ligands. *Biophys. J.* **92**, 2964-2974. doi:10.1529/biophysj.106.089730

Chan, C. E. and Odde, D. J. (2008). Traction dynamics of filopodia on compliant substrates. *Science* **322**, 1687-1691. doi:10.1126/science.1163595

Chen, S., Fu, P., Cong, R., Wu, H. S. and Pei, M. (2015). Strategies to minimize hypertrophy in cartilage engineering and regeneration. *Genes Dis.* **2**, 76-95. doi:10.1016/j.gendis.2014.12.003

Choi, S., Yu, J., Kim, W. and Park, K.-S. (2021). N-cadherin mediates the migration of bone marrow-derived mesenchymal stem cells toward breast tumor cells. *Theranostics* **11**, 6786-6799. doi:10.7150/thno.59703

Cluzel, C., Saltel, F., Lussi, J., Paulhe, F., Imhof, B. A. and Wehrle-Haller, B. (2005). The mechanisms and dynamics of αvβ3 integrin clustering in living cells. *J. Cell Biol.* **171**, 383-392. doi:10.1083/jcb.200503017

Coelho, C. N. D. and Kosher, R. A. (1991). Gap junctional communication during limb cartilage differentiation. *Dev. Biol.* **144**, 47-53. doi:10.1016/0012-1606(91)90477-K

Davidson, L. A., Hoffstrom, B. G., Keller, R. and Desimone, D. W. (2002). Mesendoderm extension and mantle closure in Xenopus laevis gastrulation: combined roles for integrin α5β1, fibronectin, and tissue geometry. *Dev. Biol.* **242**, 109-129. doi:10.1006/dbio.2002.0537

Delise, A. M. and Tuan, R. S. (2002). Alterations in the spatiotemporal expression pattern and function of N-cadherin inhibit cellular condensation and chondrogenesis of limb mesenchymal cells in vitro. *J. Cell. Biochem.* **87**, 342-359. doi:10.1002/jcb.10308

Delise, A. M., Fischer, L. and Tuan, R. S. (2000). Cellular interactions and signaling in cartilage development. *Osteoarthr. Cartil.* **8**, 309-334. doi:10.1053/joca.1999.0306

Dickinson, R. B. and Tranquillo, R. T. (1993). Optimal estimation of cell movement indices from the statistical analysis of cell tracking data. *AIChe J.* **39**, 1995-2010. doi:10.1002/aic.690391210

Dieterich, P., Klages, R., Preuss, R. and Schwab, A. (2008). Anomalous dynamics of cell migration. *Proc. Natl. Acad. Sci. USA* **105**, 459-463. doi:10.1073/pnas.0707603105

Dimilla, P. A., Stone, J. A., Quinn, J. A., Albelda, S. M. and Lauffenburger, D. A. (1993). Maximal migration of human smooth muscle cells on fibronectin and type IV collagen occurs at an intermediate attachment strength. *J. Cell Biol.* **122**, 729-737. doi:10.1083/jcb.122.3.729

Elosegui-Artola, A., Bazellières, E., Allen, M. D., Andreu, I., Oria, R., Sunyer, R., Gomm, J. J., Marshall, J. F., Jones, J. L., Trepat, X. et al. (2014). Rigidity sensing and adaptation through regulation of integrin types. *Nat. Mater.* **13**, 631-637. doi:10.1038/nmat3960

Erez, N., Zamir, E., Gour, B. J., Blaschuk, O. W. and Geiger, B. (2004). Induction of apoptosis in cultured endothelial cells by a cadherin antagonist peptide: Involvement of fibroblast growth factor receptor-mediated signalling. *Exp. Cell Res.* **294**, 366-378. doi:10.1016/j.yexcr.2003.11.033

Evans, M. S. and Tuan, R. S. (1988). Cellular condensation and collagen Type II expression during chondrogenesis in vitro. *J. Cell Biol.* **107**, 163a.

Friedl, P., Entschladen, F., Conrad, C., Niggemann, B. and Zänker, K. S. (1998). CD4+ T lymphocytes migrating in three-dimensional collagen lattices lack focal adhesions and utilize beta1 integrin independent strategies for polarization, interaction with collagen fibers and locomotion. *Eur. J. Immunol.* **28**, 2331-2343. doi:10.1002/(SICI)1521-4141(199808)28:08<2331::AID-IMMU2331>3.0.CO;2-C

Gago-Fuentes, R., Bechberger, J. F., Varela-Eirin, M., Varela-Vazquez, A., Acea, B., Fonseca, E., Naus, C. C. and Mayan, M. D. (2016). The C-terminal domain of connexin43 modulates cartilage structure via chondrocyte phenotypic changes. *Oncotarget* **7**, 73055-73067. doi:10.18632/oncotarget.12197

Giffin, J. L., Gaitor, D. and Franz-Odendaal, T. A. (2019). The forgotten skeletogenic condensations: A comparison of early skeletal development amongst vertebrates. *J. Dev. Biol.* **7**, 4. doi:10.3390/jdb7010004

Graziani, V., Rodriguez-Hernandez, I., Maiques, O. and Sanz-Moreno, V. (2022). The amoeboid state as part of the epithelial-to-mesenchymal transition programme. *Trends Cell Biol.* **32**, 228-242. doi:10.1016/j.tcb.2021.10.004

Guan, X., Wilson, S., Schlender, K. K. and Ruch, R. J. (1996). Gap-junction disassembly and connexin 43 dephosphorylation induced by 18β-glycyrrhetinic acid. *Mol. Carcinog.* **16**, 157-164. doi:10.1002/(SICI)1098-2744(199607)16:3<157::AID-MC6>3.0.CO;2-E

Hennig, K., Wang, I., Moreau, P., Valon, L., Debeco, S., Coppey, M., Miroshnikova, Y. A., Albiges-Rizo, C., Favard, C., Voituriez, R. et al. (2020). Stick-slip dynamics of cell adhesion triggers spontaneous symmetry breaking and directional migration of mesenchymal cells on one-dimensional lines. *Sci. Adv.* **6**, eaau5670. doi:10.1126/sciadv.aau5670

Humphries, J. D., Byron, A. and Humphries, M. J. (2006). Integrin ligands at a glance. *J. Cell Sci.* **119**, 3901-3903. doi:10.1242/jcs.03098

Janners, M. Y. and Searls, R. L. (1970). Changes in rate of cellular proliferation during the differentiation of cartilage and muscle in the mesenchyme of the embryonic chick. *Dev. Biol.* **23**, 136-165. doi:10.1016/S0012-1606(70)80011-2

Kalson, N., Lu, Y., Taylor, S. H., Starborg, T., Holmes, D. F. and Kadler, K. (2015). A structure-based extracellular matrix expansion mechanism of fibrous tissue growth. *Elife* **4**, e05958. doi:10.7554/eLife.05958

Kawaguchi, K., Kageyama, R. and Sano, M. (2017). Topological defects control collective dynamics in neural progenitor cell cultures. *Nature* **545**, 327-331. doi:10.1038/nature22321

Klank, R. L., Decker Grunke, S. A., Bangasser, B. L., Forster, C. L., Price, M. A., Odde, T. J., Santacruz, K. S., Rosenfeld, S. S., Canoll, P., Turley, E. A. et al. (2017). Biphasic dependence of Glioma survival and cell migration on CD44 expression level. *Cell Rep.* **18**, 23-31. doi:10.1016/j.celrep.2016.12.024

Koteliansky, V. E., Bejanian, M. V. and Smirnov, V. N. (1980). Electron microscopy study of fibronectin structure. *FEBS Lett.* **120**, 283-286. doi:10.1016/0014-5793(80)80317-6

Lagunas, A., Castaño, A. G., Artés, J. M., Vida, Y., Collado, D., Pérez-Inestrosa, E., Gorostiza, P., Claros, S., Andrades, J. A. and Samitier, J. (2014). Large-scale dendrimer-based uneven nanopatterns for the study of local arginine-glycine-aspartic acid (RGD) density effects on cell adhesion. *Nano Res.* **7**, 399-409. doi:10.1007/s12274-014-0406-2

Lagunas, A., Tsintzou, I., Vida, Y., Collado, D., Pérez-Inestrosa, E., Rodríguez Pereira, C., Magalhaes, J., Andrades, J. A. and Samitier, J. (2017). Tailoring RGD local surface density at the nanoscale toward adult stem cell chondrogenic commitment. *Nano Res.* **10**, 1959-1971. doi:10.1007/s12274-016-1382-5

Lämmermann, T. and Sixt, M. (2009). Mechanical modes of 'amoeboid' cell migration. *Curr. Opin. Cell Biol.* **21**, 636-644. doi:10.1016/j.ceb.2009.05.003

Li, L., Norrelykke, S. F. and Cox, E. C. (2008). Persistent cell motion in the absence of external signals: a search strategy for eukaryotic cells. *PLoS One* **3**, e2093. doi:10.1371/journal.pone.0002093

Li, A., Cho, J.-H., Reid, B., Tseng, C.-C., He, L., Tan, P., Yeh, C.-Y., Wu, P., Li, Y., Widelitz, R. B. et al. (2018). Calcium oscillations coordinate feather mesenchymal cell movement by SHH dependent modulation of gap junction networks. *Nat. Commun.* **9**, 5377. doi:10.1038/s41467-018-07661-5

Liu, Y.-J., Le Berre, M., Lautenschlaeger, F., Maiuri, P., Callan-Jones, A., Heuzé, M., Takaki, T., Voituriez, R. and Piel, M. (2015). Confinement and low adhesion induce fast amoeboid migration of slow mesenchymal cells. *Cell* **160**, 659-672. doi:10.1016/j.cell.2015.01.007

Luga, V., Zhang, L., Viloria-Petit, A. M., Ogunjimi, A. A., Inanlou, M. R., Chiu, E., Buchanan, M., Hosein, A. N., Basik, M. and Wrana, J. L. (2012). Exosomes mediate stromal mobilization of autocrine Wnt-PCP signaling in breast cancer cell migration. *Cell* **151**, 1542-1556. doi:10.1016/j.cell.2012.11.024

Madl, C. M., Lesavage, B. L., Dewi, R. E., Dinh, C. B., Stowers, R. S., Khariton, M., Lampe, K. J., Nguyen, D., Chaudhuri, O., Enejder, A. et al. (2017). Maintenance of neural progenitor cell stemness in 3D hydrogels requires matrix remodelling. *Nat. Mater.* **16**, 1233-1242. doi:10.1038/nmat5020

Madl, C. M., Lesavage, B. L., Dewi, R. E., Lampe, K. J. and Heilshorn, S. C. (2019). Matrix remodeling enhances the differentiation capacity of neural progenitor cells in 3D hydrogels. *Adv. Sci.* **6**, 1801716. doi:10.1002/advs.201801716

Mayan, M. D., Gago-Fuentes, R., Carpintero-Fernandez, P., Fernandez-Puente, P., Filgueira-Fernandez, P., Goyanes, N., Valiunas, V., Brink, P. R., Goldberg, G. S. and Blanco, F. J. (2015). Articular chondrocyte network mediated by gap junctions: Role in metabolic cartilage homeostasis. *Ann. Rheum. Dis.* **74**, 275-284. doi:10.1136/annrheumdis-2013-204244

Miura, T. and Shiota, K. (2000). TGFβ2 acts as an "activator" molecule in reaction–diffusion model and is involved in cell sorting phenomenon in mouse limb micromass culture. *Dev. Dyn.* **217**, 241-249. doi:10.1002/(SICI)1097-0177(200003)217:3<241::AID-DVDY2>3.0.CO;2-K

Moreno-Layseca, P., Icha, J., Hamidi, H. and Ivaska, J. (2019). Integrin trafficking in cells and tissues. *Nat. Cell Biol.* **21**, 122-132. doi:10.1038/s41556-018-0223-z

Newman, S. A. and Tomasek, J. J. (1996). Morphogenesis of connective tissues. In *Extracellular Matrices*, Vol. 2, (ed. W.D. Comper), pp. 335-369. Peading, MA: Harwood Academic Publishers.

Oberlender, S. A. and Tuan, R. S. (1994). Expression and functional involvement of N-cadherin in embryonic limb chondrogenesis. *Development* **120**, 177-187. doi:10.1242/dev.120.1.177

Oria, R., Wiegand, T., Escribano, J., Elosegui-Artola, A., Uriarte, J. J., Moreno-Pulido, C., Platzman, I., Delcanale, P., Albertazzi, L., Navajas, D. et al. (2017). Force loading explains spatial sensing of ligands by cells. *Nature* **552**, 219-224. doi:10.1038/nature24662

Paňková, K., Rösel, D., Novotný, M., Brábek, and J. , (2010). The molecular mechanisms of transition between mesenchymal and amoeboid invasiveness in tumor cells. *Cell. Mol. Life Sci.* **2010**, 63-71. doi:10.1007/s00018-009-0132-1

Pogoda, K., Kameritsch, P., Retamal, M. A. and Vega, J. L. (2016). Regulation of gap junction channels and hemichannels by phosphorylation and redox changes: a revision. *BMC Cell Biol.* **17**, 137-150. doi:10.1186/s12860-016-0099-3

Renkawitz, J., Schumann, K., Weber, M., Lämmermann, T., Pflicke, H., Piel, M., Polleux, J., Spatz, J. P. and Sixt, M. (2009). Adaptive force transmission in amoeboid cell migration. *Nat. Cell Biol.* **11**, 1438-1443. doi:10.1038/ncb1992

Roycroft, A., Szabó, A., Bahm, I., Daly, L., Charras, G., Parsons, M. and Mayor, R. (2018). Redistribution of adhesive forces through Src/FAK drives contact inhibition of locomotion in neural crest. *Dev. Cell* **45**, 565-579.e3. doi:10.1016/j.devcel.2018.05.003

Ruprecht, V., Wieser, S., Callan-Jones, A., Smutny, M., Morita, H., Sako, K., Barone, V., Ritsch-Marte, M., Sixt, M., Voituriez, R. et al. (2015). Cortical contractility triggers a stochastic switch to fast amoeboid cell motility. *Cell* **160**, 673-685. doi:10.1016/j.cell.2015.01.008

San Antonio, J. D. and Tuan, R. S. (1986). Chondrogenesis of limb bud mesenchyme in vitro: stimulation by cations. *Dev. Biol.* **115**, 313-324. doi:10.1016/0012-1606(86)90252-6

Scarpa, E. and Mayor, R. (2016). Collective cell migration in development. *J. Cell Biol.* **212**, 143-155. doi:10.1083/jcb.201508047

Shintani, Y., Fukumoto, Y., Chaika, N., Grandgenett, P. M., Hollingsworth, M. A., Wheelock, M. J. and Johnson, K. R. (2008). ADH-1 suppresses *N*-cadherin-dependent pancreatic cancer progression. *Int. J. Cancer* **77**, 71-77. doi:10.1002/ijc.23027

Singh, P. and Schwarzbauer, J. E. (2012). Fibronectin and stem cell differentiation - lessons from chondrogenesis. *J. Cell Sci.* **125**, 3703-3712. doi:10.1242/jcs.095786

Solan, J. L. and Lampe, P. D. (2014). Specific Cx43 phosphorylation events regulate gap junction turnover in vivo. *FEBS Lett.* **588**, 1423-1429. doi:10.1016/j.febslet.2014.01.049

Solan, J. L. and Lampe, P. D. (2018). Spatio-temporal regulation of connexin43 phosphorylation and gap junction dynamics. *Biochim. Biophys. Acta* **1860**, 83-90. doi:10.1016/j.bbamem.2017.04.008

Stramer, B. and Mayor, R. (2017). Mechanisms and in vivo functions of contact inhibition of locomotion. *Nat. Rev. Mol. Cell Biol.* **18**, 43-55. doi:10.1038/nrm.2016.118

Sung, B. H., Ketova, T., Hoshino, D., Zijlstra, A. and Weaver, A. M. (2015). Directional cell movement through tissues is controlled by exosome secretion. *Nat. Commun.* **6**, 7164. doi:10.1038/ncomms8164

Tarantino, N., Tinevez, J.-Y., Crowell, E. F., Boisson, B., Henriques, R., Mhlanga, M., Agou, F., Israël, A. and Laplantine, E. (2014). TNF and IL-1 exhibit distinct ubiquitin requirements for inducing NEMO-IKK supramolecular structures. *J. Cell Biol.* **204**, 231-245. doi:10.1083/jcb.201307172

Theveneau, E. and Mayor, R. (2012). Cadherins in collective cell migration of mesenchymal cells. *Curr. Opin. Cell Biol.* **24**, 677-684. doi:10.1016/j.ceb.2012.08.002

Theveneau, E. and Mayor, R. (2013). Collective cell migration of epithelial and mesenchymal cells. *Cell. Mol. Life Sci.* **70**, 3481-3492. doi:10.1007/s00018-012-1251-7

Ulrich, F., Krieg, M., Schötz, E. M., Link, V., Castanon, I., Schnabel, V., Taubenberger, A., Mueller, D., Puech, P. and Heisenberg, C. (2005). Wnt11 functions in gastrulation by controlling cell cohesion through Rab5c and *E*-cadherin. *Dev. Cell* **9**, 555-564. doi:10.1016/j.devcel.2005.08.011

Wang, Z., Collighan, R. J., Gross, S. R., Danen, E. H. J., Orend, G., Telci, D. and Griffin, M. (2010). RGD-independent cell adhesion via a tissue transglutaminase-fibronectin matrix promotes fibronectin fibril deposition and requires syndecan-4/2 and α5β1 integrin co-signaling. *J. Biol. Chem.* **285**, 40212-40229. doi:10.1074/jbc.M110.123703

Widelitz, R. B., Jiang, T. X., Murray, B. A. and Chuong, C. M. (1993). Adhesion molecules in skeletogenesis: II. Neural cell adhesion molecules mediate pre-cartilaginous mesenchymal condensations and enhance chondrogenesis. *J. Cell. Physiol.* **156**, 399-411. doi:10.1002/jcp.1041560224

Williams, E., Williams, G., Gour, B. J., Blaschuk, O. W. and Doherty, P. (2000). A novel family of cyclic peptide antagonists suggests that *N*-cadherin specificity is determined by amino acids that flank the HAV motif. *J. Biol. Chem.* **275**, 4007-4012. doi:10.1074/jbc.275.6.4007

Wu, P., Giri, A. and Wirtz, D. (2015). Statistical analysis of cell migration in 3D using the anisotropic persistent random walk model. *Nat. Protoc.* **10**, 517-527. doi:10.1038/nprot.2015.030

Xiong, J. P., Stehle, T., Zhang, R. G., Joachimiak, A., Frech, M. and Goodman, S. L. and Arnaout, M. A. (2002). Crystal structure of the extracellular segment of integrin αVβ3 in complex with an Arg-Gly-Asp ligand. *Science* **296**, 151-155. doi:10.1126/science.1069040

Yamada, K. and Sixt, M. (2019). Mechanisms of 3D cell migration. *Nat. Rev. Mol. Cell Biol.* **20**, 738-752. doi:10.1038/s41580-019-0172-9

Yeoman, B. M. and Katira, P. (2019). A stochastic algorithm for accurately predicting path persistence of cells migrating in 3D matrix environments. *PLoS One* **13**, e0207216. doi:10.1371/journal.pone.0207216

Zhu, Y., Gao, C., Liu, X., He, T. and Shen, J. (2004). Immobilization of biomacromolecules onto aminolyzed Poly(L-lactic acid) toward acceleration of endothelium regeneration. *Tissue Eng.* **10**, 53-61. doi:10.1089/107632704322791691

Zisis, T., Brückner, D. B., Brandstätter, T., Siow, W. X., D'alessandro, J., Vollmar, A. M., Broedersz, C. P. and Zahler, S. (2022). Disentangling cadherin-mediated cell-cell interactions in collective cancer cell migration. *Biophys. J.* **121**, 44-60. doi:10.1016/j.bpj.2021.12.006